Article

Thermal Calibration of Triaxial Accelerometer for Tilt Measurement

Bo Yuan [1], Zhifeng Tang [2,*] , Pengfei Zhang [2] and Fuzai Lv [3]

[1] Polytechnic Institute, Zhejiang University, Hangzhou 310027, China, 22060017@zju.edu.cn
[2] College of Biomedical Engineering and Instrument Science, Zhejiang University, Hangzhou 310027, China; zhangpengfei@zju.edu.cn
[3] State Key Laboratory of Fluid Power and Mechatronic Systems, School of Mechanical Engineering, Zhejiang University, 38 Zheda Road, Hangzhou 310027, China; lfzlfz@zju.edu.cn
* Correspondence: tangzhifeng@zju.edu.cn

Abstract: This paper presents a calibration and thermal compensation method that aims to minimize cost and processing time while maintaining high accuracy. First, the number of positions to perform the calibration procedure is optimized, and then, based on this optimized calibration number, thermal compensation is performed, which is necessary for environments with large temperature variations, since calibration parameters change at different temperatures. The calibration procedures and algorithms were experimentally validated on marketed accelerometers. Based on the optimized calibration method, the calibrated results have been obtained nearly 100 times improvement. Thermal drift calibration experiments on the triaxial accelerometer show that the thermal compensation scheme in this paper can effectively reduce drift in the temperature range of -40°C to 60°C. The temperature drifts of x- and y-axes are reduced from -13.2 and 11.8 mg to -0.9 and -1.1 mg, respectively. The z-axis temperature drift is reduced from -17.9 to 1.8 mg. We have conducted various experiments on the proposed calibration method and demonstrated its capacity to calibrate the sensor frame error model (SFEM) parameters. Therefore, the MEMS sensors calibrated in this paper have certain engineering application values for tilt measurement.

Keywords: MEMS; triaxial accelerometer; error analysis; thermal drift; calibration; temperature compensation; tilt measurement

1. Introduction

Micro-electromechanical systems (MEMS) have been evolving since MEMS-based inertial sensors were widely used in commercial and military applications such as human motion tracking, navigation systems, and posture control systems [1–4]. Features such as tiny size, cost, and low energy consumption make them very attractive. Such accelerometers must be calibrated as precisely as possible because even slight biases in accelerometers can result in very quick direction drift when used for inertial navigation system (INS) applications and inaccurate tilt angle measurements [5–7]. Furthermore, the performance of these sensors is greatly dependent on external circumstances, such as temperature changes. As a result, precise, reliable, and effective thermal models are required to decrease the impact of these errors, which can degrade system performance [8–11]. Factory-based triaxial accelerometers calibration is a time-consuming and expensive process, usually performed for specific advanced sensors [12].

There are several different errors and temperature-dependent models for triaxial MEMS sensors and corresponding calibration methods based on different principles, but they have restrictions, for instance, the need to provide accurate platforms for precise alignment or other temperature compensation devices. It is not sufficient for manufacturers to perform only basic calibration of low-cost sensors, as even small uncompensated coefficients can lead to inaccurate tilt angle estimation and increased bias in position

 doi:10.20944/preprints202212.0339.v1

measurements [13–16]. These requirements increase manufacturing costs. Therefore, it is necessary to investigate alternative methods [17].

For example, the common accelerometer calibration method described by Khan and Ranj [18] uses six specific positions where the sensor axes are precisely aligned along the axis of the calibration device. The accelerometer is calibrated by a specific position with a certain reference angle. This calibration method can only estimate offset and scale factor errors, not non-orthogonality, and the accuracy of the calibration depends heavily on the accuracy of alignment with the calibration device [19]. The ellipsoidal fitting method is often used to improve calibration accuracy while reducing device costs, as presented in [20, 21]. This method combines the error parameters by fitting them to the ellipsoid data through linear regression, and then based on the calculated ellipsoid parameters, the unknown error model parameters can be estimated. Maximum likelihood estimation tackles the problem from a probabilistic perspective, but usually uses probability density functions rather than probabilities [22, 23]. The kalman filter and its extensions attempt to estimate both the error model and the calibration parameters within a calibration function based on the system model and observations over a period of time [24].

In terms of temperature compensation, the manufacturer's technical data is not sufficient for inclination measurement applications. In addition, the sensor output is affected by temperature and environmental conditions. Temperature drift, if not compensated for, will lead to attitude estimation drifts. Talha, Kivanc, and Tayfun described a temperature compensation method for a condenser MEMS accelerometer by using a MEMS dual-ended tuning fork to compensate for the temperature dependence of the accelerometer output [25]. The purpose of temperature compensation is to determine the error of the triaxial accelerometers at different temperature points. Xu described an efficient temperature compensation methodology based on neural network using the collected accelerometer responses from -30 °C to 50 °C as learning data [26]. These compensation methods require additional equipment and are capable of determining only scale factor errors and offsets.

In this paper, we aim to model the temperature compensation for a low-cost triaxial accelerometer sensor that will be used for clinometric applications. This paper is organized as follows. In Section 2, we introduce the error source of the triaxial accelerometer and describe the error model of the three-axis MEMS accelerometer, where the biases, scale factors, nonorthogonal error, and misalignments are considered thermal calibration parameters. We describe the algorithms used for its calibration and temperature compensation in Section 3. Experiments and analysis are provided in Section 4.

2. Error Source and Error Model

An accelerometer is a device that can detect force in accordance with Newton's second law of motion [27]. It is made up of a seismic mass as well as a capacitance to voltage converting circuit. When a force acts on the accelerometer, the seismic mass deflects, causing a change in capacitance as well as voltage. As with other sensors, triaxial accelerometers are subject to measurement errors due to variations in internal structure and external environment. The errors of triaxial accelerometers can be roughly divided into deterministic errors and random errors. Deterministic errors include zero bias errors, scale factor, and non-orthogonality errors. Random errors are caused by drift errors, random noise, and turn-on errors, which cannot be predicted or compensated directly [28–30].

2.1 Sensor Frame Error Model

As shown in Figure 1a, the output signal from the MEMS accelerometers should be zero when there is no signal input to the sensor, but this is not the case. This phenomenon is caused by a flaw in the manufacturing of the folded cantilever that holds the accelerometer's mass. The asymmetrically folded cantilever fails to bring the mass into equilibrium. As a result, a false differential capacitance influences the sensor electrode. A faulty suppression of parasitic capacitance in a capacitive sensor, on the other hand, introduces uncompensated biases. As shown in Figure 1b, the scale factor is the ratio of

Preprints (www.preprints.org) | NOT PEER-REVIEWED | Posted: 19 December 2022 doi:10.20944/preprints202212.0339.v1

an output change to an intended input variation. An ideal sensor has only one scale factor. The scale factor error can be introduced by flaws in the manufacturing of the folded cantilever and the process of weak signal detection and extraction. Each sensitive axis' scale factor can be expressed as a series of coefficients. As shown in Figure 1c, ideally, the triaxial accelerometer sensitivity axes should be orthogonal, but inaccuracies in the internal construction of the chip can cause non-orthogonal errors between the axes. MEMS sensors output a voltage that is proportional to the acceleration detected by the sensor. As shown in Figure 1d, when the triaxial accelerometer is installed in an inclinometer, the three sensitive axes should be aligned with the three orthogonal axes of the body frame. In practice, however, misalignment errors occur due to errors in the sensor mounting process [31,32]. To ensure that the orthogonal output readings are displayed correctly with the sensor frame by the nonorthogonal triaxial accelerometer, misalignment errors θ, φ, and ψ must be estimated.

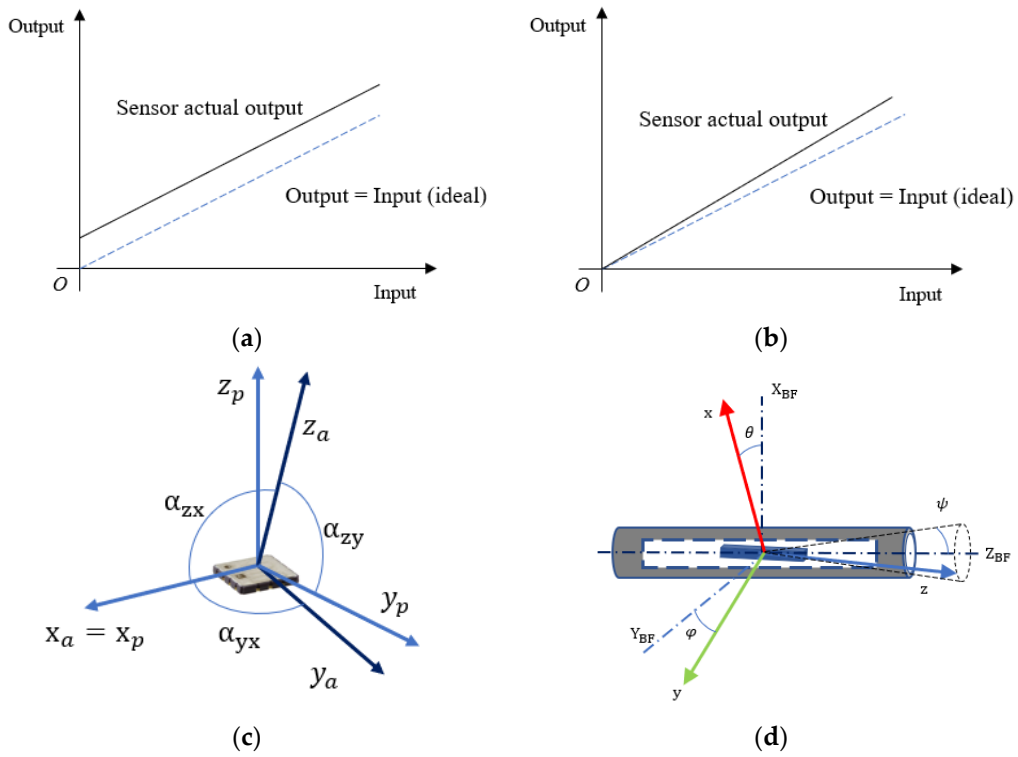

Figure 1. Sensor frame error model of triaxial accelerometer. (**a**) Zero bias error; (**b**) Scale factor error; (**c**) Nonorthogonality error; (**d**) Misalignment error.

For triaxial accelerometers, we define the SFEM for the calibration of triaxial MEMS accelerometers. Based on the above analysis of various error characteristics of the triaxial accelerometers, the SEFM can be defined as:

$$U_{SF}=M_{SF}C_{SF}S_{SF}\,(U-b_{SF})$$
$$=\begin{pmatrix} m_{xx} & m_{xy} & m_{xz} \\ m_{yx} & m_{yy} & m_{yz} \\ m_{zx} & m_{yz} & m_{zz} \end{pmatrix}\begin{pmatrix} 1 & 0 & 0 \\ \alpha_{yx} & 1 & 0 \\ \alpha_{zx} & \alpha_{zy} & 1 \end{pmatrix}\begin{pmatrix} S_{ax} & 0 & 0 \\ 0 & S_{ay} & 0 \\ 0 & 0 & S_{az} \end{pmatrix}\left(\begin{pmatrix} U_x \\ U_y \\ U_z \end{pmatrix}-\begin{pmatrix} b_x \\ b_y \\ b_z \end{pmatrix}\right) \quad (1)$$

where $U_{SF} = [X_{SF}, Y_{SF}, Z_{SF}]^T$ is the vector of accelerations after calibration; M_{SF} is the matrix describing the misaligned errors; C_{SF} is the matrix providing the conversion from non-orthogonal to orthogonal frames with non-diagonal angles α_{yx}, α_{zx}, α_{zy} corresponding to the triaxial misalignment; S_{SF} is a scale factor parameter matrix; $U = [U_x, U_y, U_z]^T$ is the vector of raw sensor readings; $b_{SF} = [b_x, b_y, b_z]^T$ is the vector of sensor offsets.

Preprints (www.preprints.org) | NOT PEER-REVIEWED | Posted: 19 December 2022 doi:10.20944/preprints202212.0339.v1

2.2 Temperature Dependence

Thermal drift of MEMS errors are typically considered deterministic errors. The following two methods are required to decrease the thermal drift of sensor errors:

1. Temperature calibration: developing accurate and reliable thermal models of the sensor errors, i.e. establishing a relationship between the sensor errors and the sensor temperature;
2. Temperature compensation: compensating the thermal drift of the sensor errors based on their temperature during the accelerometer's operation process. Both of these processes are dependent on the temperature generated by the accelerometer's internal temperature sensors.

Considering thermal errors, because temperature variations affect the internal structure of the triaxial accelerometer, the error parameters of the triaxial accelerometer vary nonlinearly with temperature [33]. Considering the temperature factor, we redefine Equation (1) as

$$U_{SF}(T) = M_{SF}(T)C_{SF}(T)S_{SF}(T)\ (U\text{-}b_{SF}(T)) \quad (2)$$

In the above formula, T represents the temperature measured by the thermal sensor. $M_{SF}(T)$, $S_{SF}(T)$, $C_{SF}(T)$, and $b_{SF}(T)$ are the coefficients that change with temperature in Equation (1). $U_{SF}(T)$ represents the output data at temperature T, and U is the vector of raw sensor readings.

3. Calibration Method

This section relies on triaxial accelerometer calibration and temperature compensation algorithms. The basic principle of calibration and compensation is based on the principle that triaxial acceleration should be calculated on the same order of magnitude as gravity in Equation (3):

$$G = \sqrt{X_{SF}^2 + Y_{SF}^2 + Z_{SF}^2} \quad (3)$$

where X_{SF}^2, Y_{SF}^2, and Z_{SF}^2 are the accelerations present in the sensor frame axes; G is the gravitational acceleration, ideally equal to 1g.

3.1. Levenberg-Marquardt algorithm

The Levenberg-Marquardt (LM) algorithm is one of the most efficient and widely used algorithms and is often used to solve nonlinear least squares problems. It is more robust than the Gause-Newton (GN) algorithm. The Levenberg-Marquardt algorithm combines two numerical optimization algorithms: the Gradient Descent (GD) method and the Gauss-Newton (GN) method [34–36]. To obtain the most precise coefficients without using a highly accurate turntable system, the triaxial accelerometer should be placed continuously and fixed to cover the entire surface of the sphere, and the accelerometer should be influenced only by gravity during the experiment. However, this is not possible in practice, because the measurement sum for this calibration method would be infinite. So we try to test and optimize the number of positions for compensation during the calibration. In [37], the 24-position method was used, as shown in Table 1 for three directions along the x, y, and z axes, with eight positions in each direction. The calibration method can be described as (4).

$$S(\beta) = \sum_{i=1}^{m} [y_i - f(x_i, \beta)]^2 \quad (4)$$

Where $S(\beta)$ denotes the sum of $[y_i - f(x_i, \beta)]^2$; m is the measurement number; x_i is the measured value; y_i are the reference acceleration data, and β is a parameter vector as defined in Equation (1).

Here we use the Levenberg-Marquardt algorithm, which reduces $S(\beta)$ with respect to the parameters in vector β.

Preprints (www.preprints.org) | NOT PEER-REVIEWED | Posted: 19 December 2022 doi:10.20944/preprints202212.0339.v1

1) The Gradient Descent Method: The Gradient Descent (GD) algorithm is a commonly used minimization method that updates the parameter values in the opposite direction of the gradient from the objective function. The GD algorithm is highly convergent and can be used for optimization problems with thousands of parameters. The GD algorithm update h_{gd} that modifies the $S(\beta)$ in the direction of the steepest descent can be defined as shown in Equation (5).

$$h_{gd} = \alpha J^T W\left(y_i - f(x_i, \beta)\right) \quad (5)$$

Where α is a positive scalar corresponding to the step in the steepest-descent direction; J is a Jacobian matrix based on the vector β; W can be set as the inverse matrix of the measurement error covariance matrix.

2) The Gauss-Newton Method: The Gauss-Newton method is a method for the minimization of the sum-of-squares target function. For medium-sized problems, the Gauss-Newton method usually converges faster than the gradient descent method. The formula for the GN algorithm to reduce $S(\beta)$ is given by the following Equation (6).

$$[J^T W J]\ h_{gn} = J^T W[y_i - f(x_i, \beta)] \quad (6)$$

Where h_{gn} indicates the GN algorithm update of the parameter estimated to lead to the minimization of $S(\beta)$.

3) The Levenberg-Marquardt method: The Levenberg-Marquardt algorithm adaptively changes the parameter updates between gradient descent parameter iterations and Gauss-Newton parameter iterations to achieve optimal progress in the minimization of $S(\beta)$. The LM algorithm can be described by Equation (7).

$$[J^T W J + \lambda \mathrm{diag}(J^T W J)]h_{lm} = J^T W[y_i - f(x_i, \beta)] \quad (7)$$

Where J is the Jacobian matrix of vectors β; W is the weighting diagonal matrix; h_{lm} is adaptively weighted to reach optimal progress in $S(\beta)$ minimization. The damping factor λ is adjusted at each iteration.

3.2. Least-Squares Fitting of Data by Polynomials

The temperature dependence of MEMS accelerometers can be defined as the nonlinear change of calibration parameters with temperature [38]. For temperature compensation, we convert the error coefficients into variables that change with temperature, which will vary according to the environment and other instrumental conditions. Polynomial regression methods are utilized in this research to model triaxial accelerometer errors based on temperature [39]. The calibration parameters in Equation (1) can be fitted with a three-dimensional polynomial as shown in Equation (8).

$$p(t) = a_0 + a_1 f(t) + a_2 f(t^2) + a_3 f(t^3) \quad (8)$$

where $p(t)$ is the calibration coefficients in (1); t is the temperature coefficient, a_0, a_1, a_2, a_3 are the fitting coefficients.

Preprints (www.preprints.org) | NOT PEER-REVIEWED | Posted: 19 December 2022 doi:10.20944/preprints202212.0339.v1

Table 1. Suggested Calibration Positions.

No.	X Axis Position	Y Axis Position	Z Axis Position
1	P_{x1} ≈ horizontal	P_{y1} ≈ vertical	P_{z1} ≈ horizontal
2	P_{x1} + 45°	P_{y1} + 45°	P_{z1}
3	P_{x1} + 90°	P_{y1} + 90°	P_{z1}
4	P_{x1} + 135°	P_{y1} + 135°	P_{z1}
5	P_{x1} + 180°	P_{y1} + 180°	P_{z1}
6	P_{x1} + 225°	P_{y1} + 225°	P_{z1}
7	P_{x1} + 270°	P_{y1} + 270°	P_{z1}
8	P_{x1} + 315°	P_{y1} + 315°	P_{z1}
9	P_{x2} ≈ horizontal	P_{y2} ≈ horizontal	P_{z2} ≈ vertical
10	P_{x2} + 45°	P_{y2}	P_{z2} + 45°
11	P_{x2} + 90°	P_{y2}	P_{z2} + 90°
12	P_{x2} + 135°	P_{y2}	P_{z2} + 135°
13	P_{x2} + 180°	P_{y2}	P_{z2} + 180°
14	P_{x2} + 225°	P_{y2}	P_{z2} + 225°
15	P_{x2} + 270°	P_{y2}	P_{z2} + 270°
16	P_{x2} + 315°	P_{y2}	P_{z2} + 315°
17	P_{x3} ≈ horizontal	P_{y3} ≈ horizontal	P_{z3} ≈ vertical
18	P_{x3}	P_{y3} + 45°	P_{z3} + 45°
19	P_{x3}	P_{y3} + 90°	P_{z3} + 90°
20	P_{x3}	P_{y3} + 135°	P_{z3} + 135°
21	P_{x3}	P_{y3} + 180°	P_{z3} + 180°
22	P_{x3}	P_{y3} + 225°	P_{z3} + 225°
23	P_{x3}	P_{y3} + 270°	P_{z3} + 270°
24	P_{x3}	P_{y3} + 315°	P_{z3} + 315°

4. Experiments and Results

4.1. Calibrated Sensors And Measurement Setup

In this section, we will briefly describe the system (Figure 2) used for calibration and temperature compensation. The performance parameters of the triaxial accelerometer are shown in Table 2. A 3-axis position turntable equipped with a thermal chamber (see Figure 3) is used to calibrate the triaxial accelerometer sensor errors over a wide temperature range. The triaxial accelerometer is fixed in the center of the triaxial turntable by using a clamp, and the turntable is controlled according to the programmed control commands. The device specifications for the turntable and the thermal chamber are shown in Table 3.

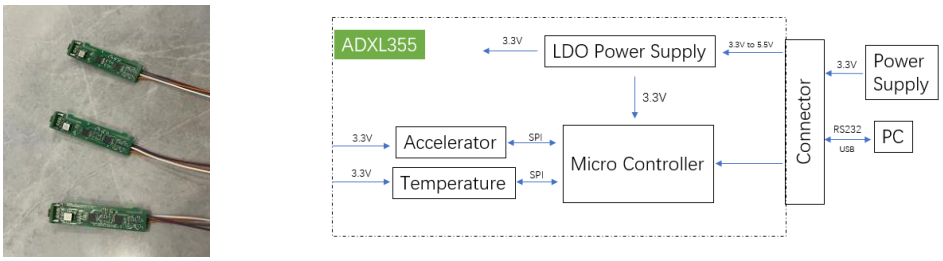

(**a**) (**b**)

Figure 2. Measurement setup for triaxial accelerometer calibration. (**a**) ADXL355 sensors; (**b**) Calibration and measurement device for triaxial accelerometer

Preprints (www.preprints.org) | NOT PEER-REVIEWED | Posted: 19 December 2022 doi:10.20944/preprints202212.0339.v1

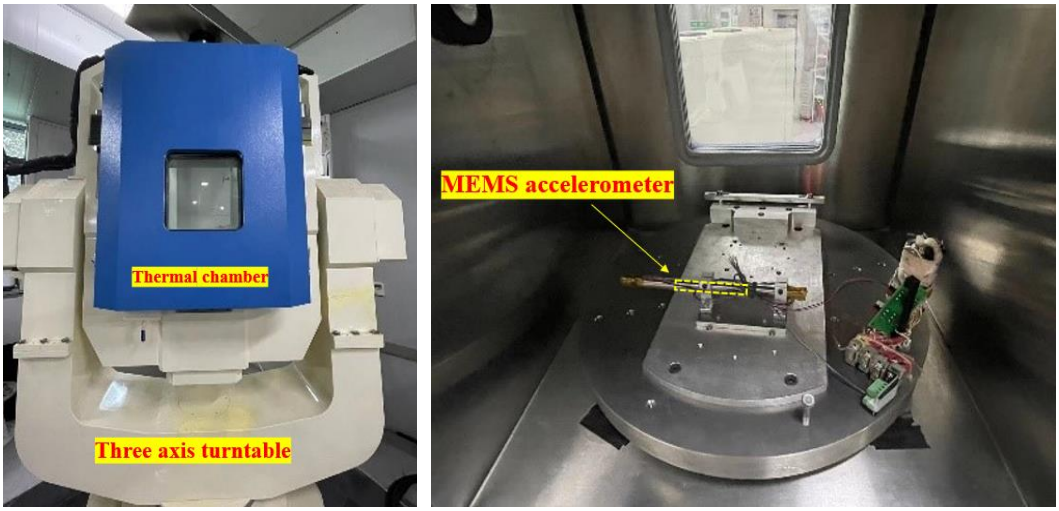

(**a**) (**b**)

Figure 3. Temperature-controlled rotational-tilt platform. **(a)** External View**; (b)** Internal View.

Table 2. Characteristics of tested ADXL355.

Specification	Value
Interface	Digital
Noise-Density ($\mu g/\sqrt{Hz}$)	25
0 g Offset (mg)	±25
Range (g)	±2/±4/±8
ADC	20-bit
Output Data Rate (Hz)	0 ~ 4000 Hz

Table 3. Performance of thermal calibration equipment.

Turntable	
Principal axis rotation range	Continuous infinite
Tilting axis angular position accuracy	±3″
Principal axis angular position accuracy	±3″
Non-orthogonalities between axes	±5″
Tilting axis rotation range	±90°
Thermal Chamber	
Temperature range	−55 ~ +100 °C
Temperature change rate	±0.1 ~ ±5 °C/min linear

4.2. Sensor Frame Error Models Analyses

For compensation purposes and sequential testing, we measured the raw data of the accelerometers at 1296 locations distributed uniformly over the sphere (Figure 4). This number is based on the number of calibration positions suggested in Section 3 multiplied by 54 for calibration position optimization. Then we analyze the dependence of the calibrated SFEM on the number of calibration positions.

The three-axis sensor is oriented in each direction as measurements are taken. The calibration device is set to stay at each position for a while and calculate the average of 200 measurement data samples to minimize sensor noise [40]. The impact of calibration on the measured data is shown in Figures 5 and 6, where the deviation of the calibrated acceleration reading from 1g is approximately 100 times smaller than the data before calibration.

Preprints (www.preprints.org) | NOT PEER-REVIEWED | Posted: 19 December 2022 doi:10.20944/preprints202212.0339.v1

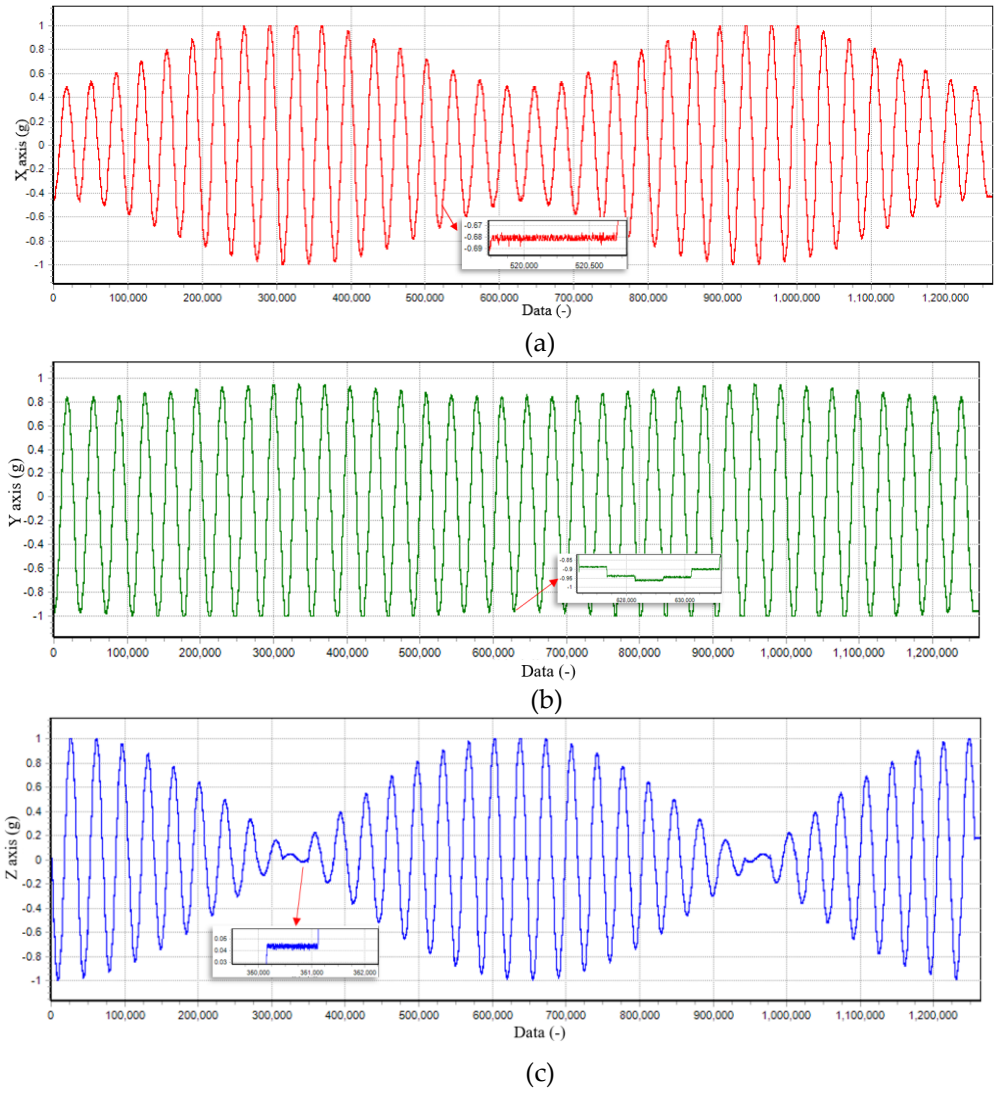

Figure 4. Acceleration values during the proposed 1296 positions calibration method. (**a**) Raw data of the x-axis; (**b**) Raw data of the y-axis; (**c**) Raw data of the z-axis.

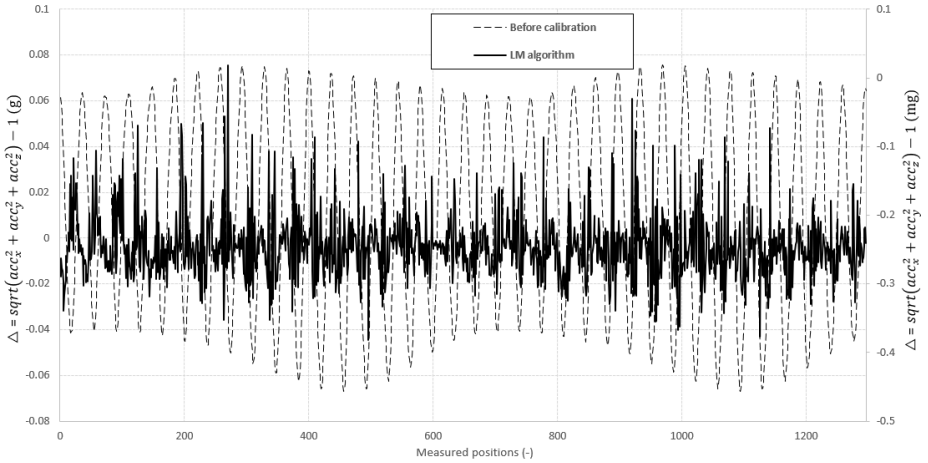

Figure 5. Analysis of the calibration between acceleration deviations observed at various points before (left vertical axis) and after (right vertical axis) calibration

Calibration parameters are estimated and used to remove the errors from the raw data. Figure 6 displays the raw data as well as the final calibrated data, together with the estimation of the ellipsoid and sphere [41].

Preprints (www.preprints.org) | NOT PEER-REVIEWED | Posted: 19 December 2022 doi:10.20944/preprints202212.0339.v1

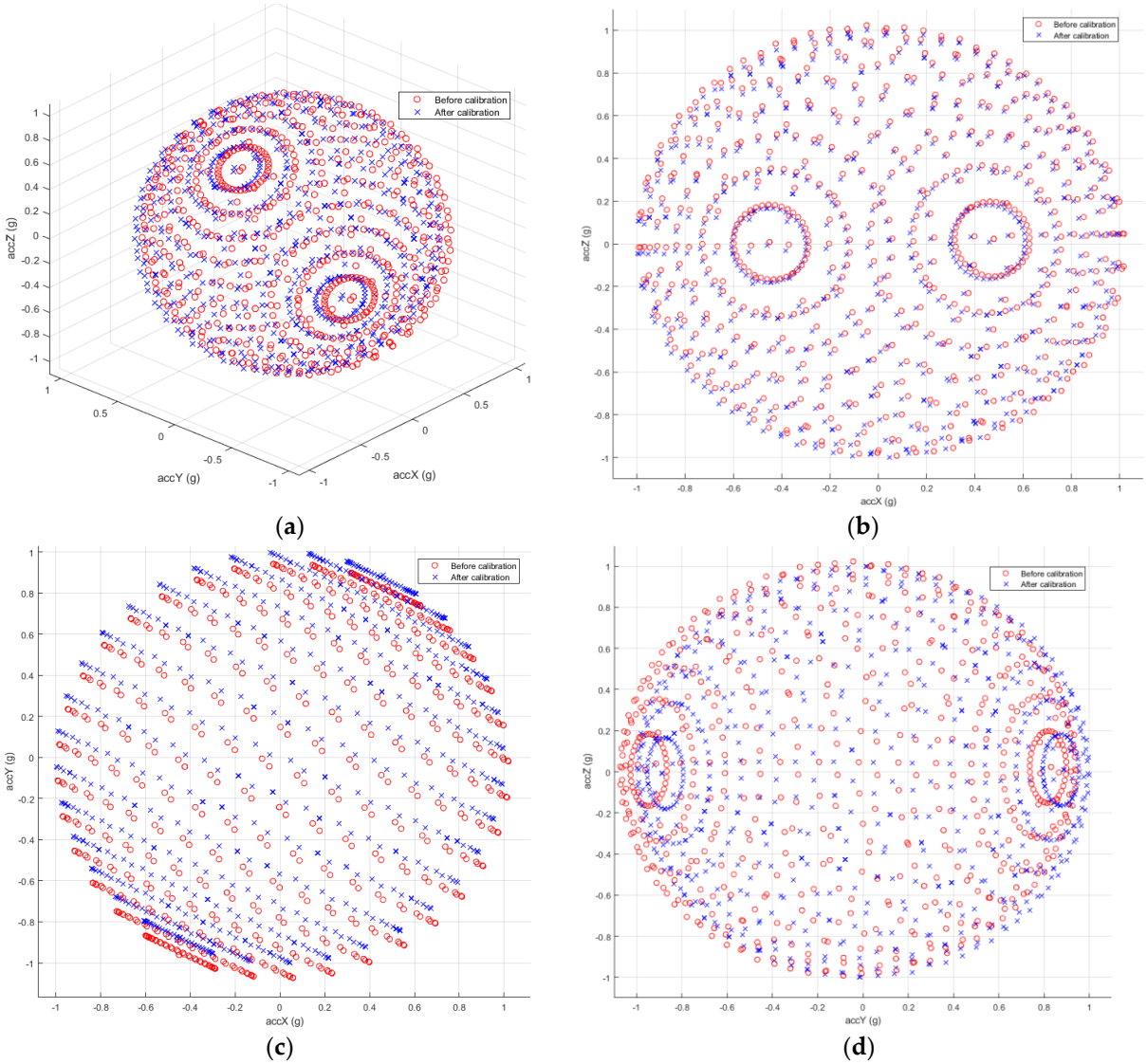

Figure 6. The 3D graphics of measured accelerations before (red 'o') and after (blue 'x') calibration. (**a**) Main View (**b**) Front view (**c**) End view (**d**) Vertical view

The LM algorithm was used to estimate the SFEM from the measurement values of the proposed positions. It contributed to reducing the influence of manufacturing defects on sensor accuracy. To achieve the optimization of the number of positions, the Root Mean Square Error (RMSE) of the comparison defined in (9) was used:

$$\mathrm{RMSE} = \sqrt{\frac{\sum_{i=1}^{n}(x_i - g)^2}{n}}$$
$$x_i = \sqrt{g_{xi}^2 + g_{yi}^2 + g_{zi}^2} \quad (9)$$

Where n is the number of positions; g is numerically the same as gravity and is equal to 1g; g_{xi}, g_{yi}, and g_{zi} are the components of gravity along each axis.

To demonstrate that 24 positions are adequate for compensation goals, we evaluated the RMSE of the SFEM from 12 to 1296 for various numbers of positions (NoP). The results are shown in Figure 7. In Table 4 you can find the NoP, where N indicates the quantitative relationship between the axis and the NoP used for the analysis [42].

Preprints (www.preprints.org) | NOT PEER-REVIEWED | Posted: 19 December 2022 doi:10.20944/preprints202212.0339.v1

Table 4. Relationship between the NoP and the axes

N	NoP	N	NoP	N	NoP
1	1296	6	64	11	18
2	648	7	48	12	16
3	324	8	36	13	12
4	162	9	24		
5	81	10	21		

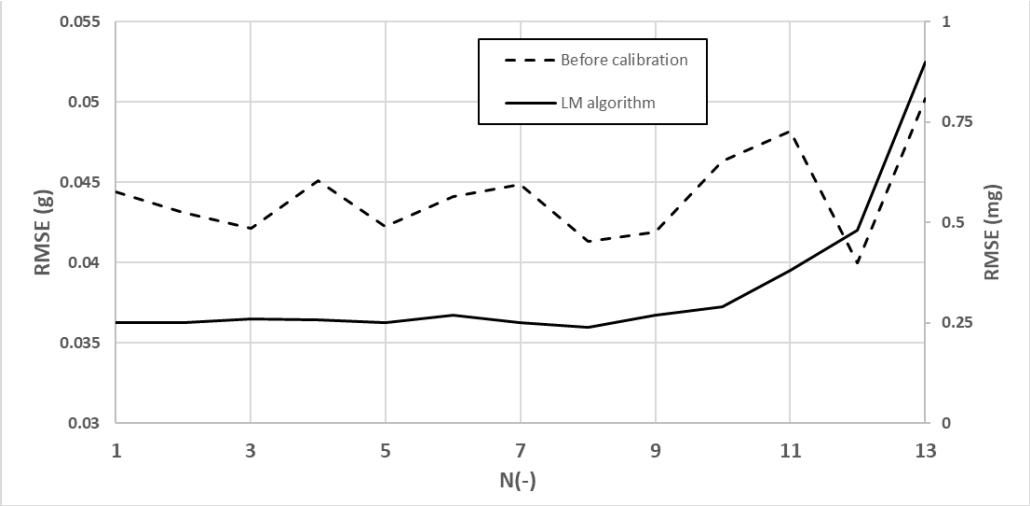

Figure 7. Relationship of RMSE before calibration (left vertical axis) and after calibration (right vertical axis)

As can be seen in Figure 7, 21 or more positions have the capacity to meet the required requirements, regardless of how many positions are rotated on the calibration device. This can also be interpreted as a variation of the compensation results below the controllable value when 21 or more positions (up to 1296) are used; therefore, we can optimize the number of calibration positions by using 24 positions to cover all axes, which is the number we used in Table 1.

After calibrating our triaxial accelerometer sensor, we fused the sensor measurements for attitude estimation using the method described in [38]. To further verify the effectiveness of the calibration, another analysis was performed where the tilt angle estimated from the calibration was compared to the reference angle measured by the Rotating Tilt Device (RTD). As shown in Figure 3b, we mounted the accelerometer on the RTD and tilted it by a specific angle along both axes. Tilt sensing measures the angle of change with respect to gravity. The output of the accelerometer sensor is read by the microcontroller's internal Analog to Digital Converter (ADC) to determine tilt. The tilt of each axis can then be calculated using the following formula (9). The tilt corresponds to the pitch angle and roll angle. The specifications are listed in Section 4 for the RTD.

$$\varphi_m = \arctan\left(-Y_{SF}/\sqrt{X_{SF}^2 + Z_{SF}^2}\right)$$
$$\theta_m = \arctan(X_{SF}/-Z_{SF}) \quad (9)$$

Where φ_m is the pitch angle; θ_m is the roll angle; X_{SF}, Y_{SF}, Z_{SF} are the measurement of the acceleration. The comparison of the tilt angle measurements before and after calibration can be seen in Table 5, where the tilt angle is more accurate than the angle without calibration due to calibration. In the last column, we use the Sensor Error Optimization Quantity (SEOQ), which is defined as the specific deviation for the difference between the two values with respect to the maximum angle, i.e., 30 degrees.

Preprints (www.preprints.org) | NOT PEER-REVIEWED | Posted: 19 December 2022 doi:10.20944/preprints202212.0339.v1

Table 5. Comparison of tilt angles before and after calibration

Reference Angle φ; θ (deg)	Without Calibration φ; θ (deg)	After Calibration φ; θ (deg)	SEOQ φ; θ (%)
0; 0	-0.77; 0.59	-0.70; -0.30	0.2; 3.0
15; 0	14.18; -0.62	14.61; -0.15	1.4; 1.6
30; 0	29.18; -0.63	30.13; 0.01	3.2; 2.1
0; -15	-0.96; -15.83	-0.91; -15.72	0.2; 0.4
0; -30	-0.82; -31.10	-0.76; -31.00	0.2; 0.3
15; -15	14.31; -15.98	14.76; -15.82	1.5; 0.5
30; -30	29.00; -29.62	29.98; -29.76	3.3; 0.5

4.3. Temperature Compensation

Based on the 24-position data measurement method described in Section 3 and demonstrated in Section 4, we conducted experiments (24 positions in our case) with temperatures cycling from -40 °C to 60 °C at 10 °C intervals, measuring the calibration coefficients at each temperature point (Figure 8).

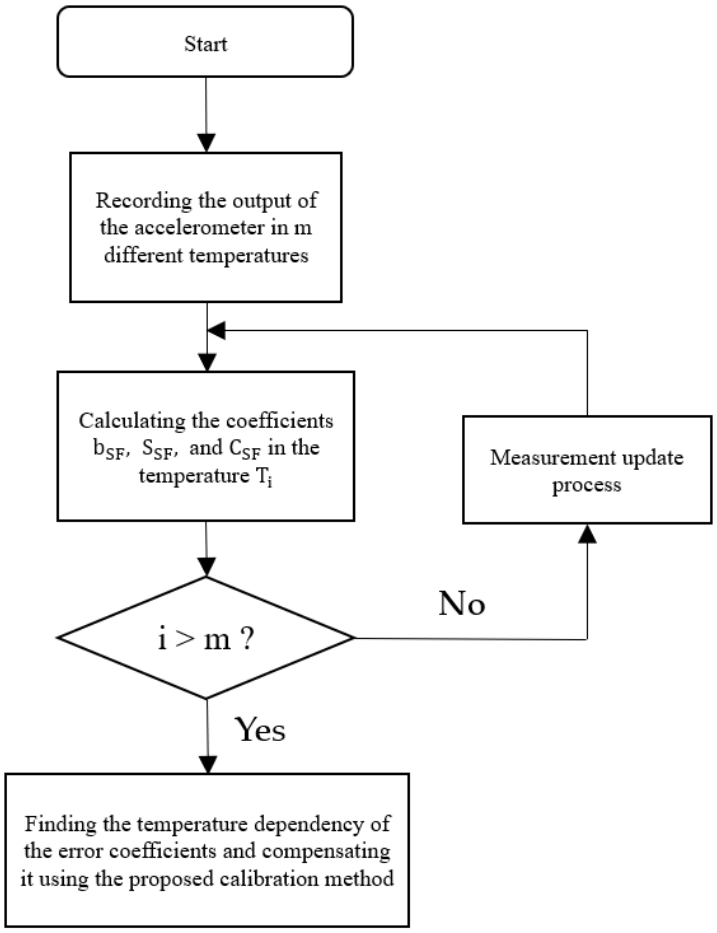

Figure 8. The estimation program routine of the triaxial accelerometer temperature coefficients.

The triaxial accelerometer is enclosed in a thermal chamber and given enough time (approximately one hour) to stabilize its temperature at the set temperature point in the temperature compensation method. The system begins recording data once the accelerometer and thermal chamber temperature have stabilized [43]. Figure 9 shows the

Preprints (www.preprints.org) | NOT PEER-REVIEWED | Posted: 19 December 2022 doi:10.20944/preprints202212.0339.v1

relationship between temperature and calibration. Due to the temperature hysteresis characteristics, we fit scatter points for temperature compensation. The analyses of the other coefficients were very similar.

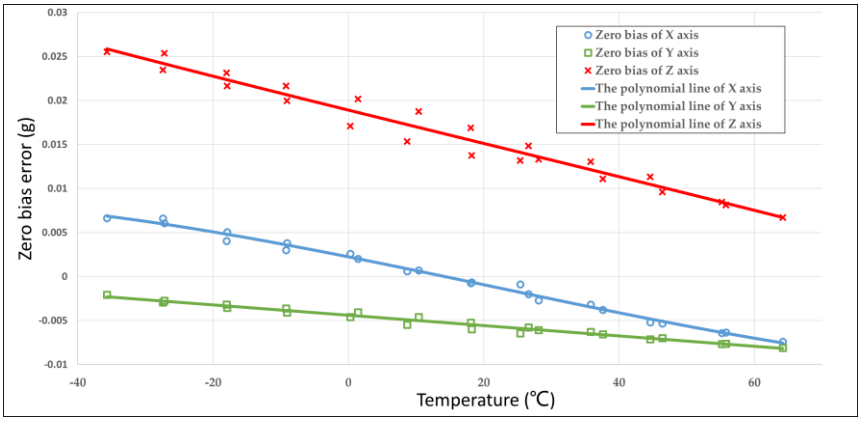

(**a**)

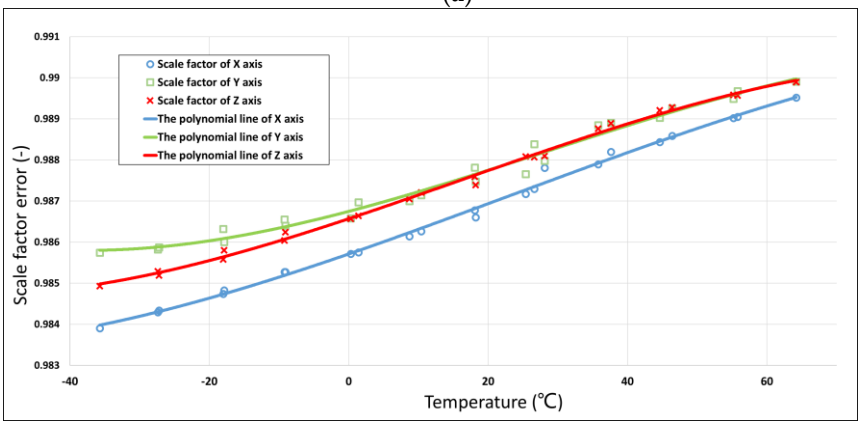

(**b**)

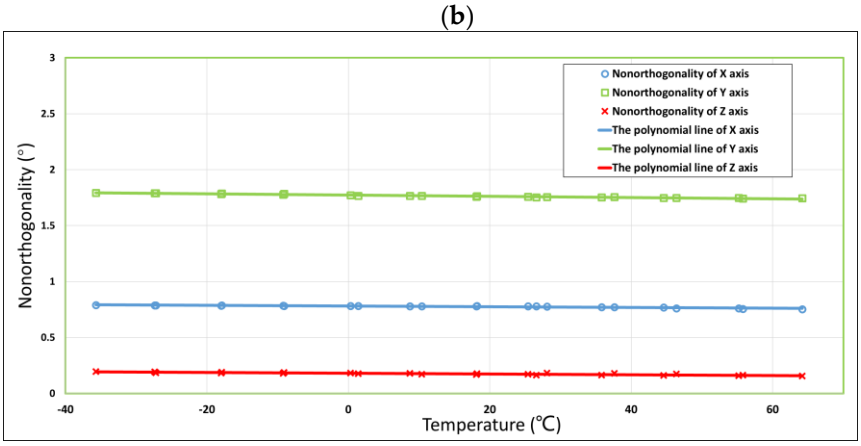

(**c**)

Figure 9. The polynomial line of each sensor axis. (**a**) Zero bias error; (**b**) Scale factor error; (**c**) Nonorthogonality error

To verify the calibration results at specific temperatures, we performed the 24-position method at some temperatures and compared the RMSE before and after calibration, as shown in Table 6.

Preprints (www.preprints.org) | NOT PEER-REVIEWED | Posted: 19 December 2022 doi:10.20944/preprints202212.0339.v1

Table 6. Comparison of RMSE before and after calibration.

Temperature (℃)	Before Calibration RMSE (mg)	Polynomial RMSE (mg)	Measurement RMSE (mg)
-35	45.1	0.19	0.17
-25	46.8	0.24	0.21
-15	47.2	0.22	0.19
-5	45.9	0.24	0.21
5	44.3	0.18	0.17
15	46.3	0.19	0.21
25	48.6	0.25	0.25
35	47.2	0.26	0.29
45	45.3	0.29	0.24
55	48.1	0.31	0.29

To verify the effect of the temperature compensation in a dynamic temperature environment, we fixed the accelerometer in a temperature-controlled oven, heated it to 60 °C, and then closed the temperature oven to allow the accelerometer to cool down naturally [44]. The compensated and uncompensated accelerometer output data can be examined in Figure 10. The temperature dependency is reduced from 1346 μg/K to 37 μg/K.

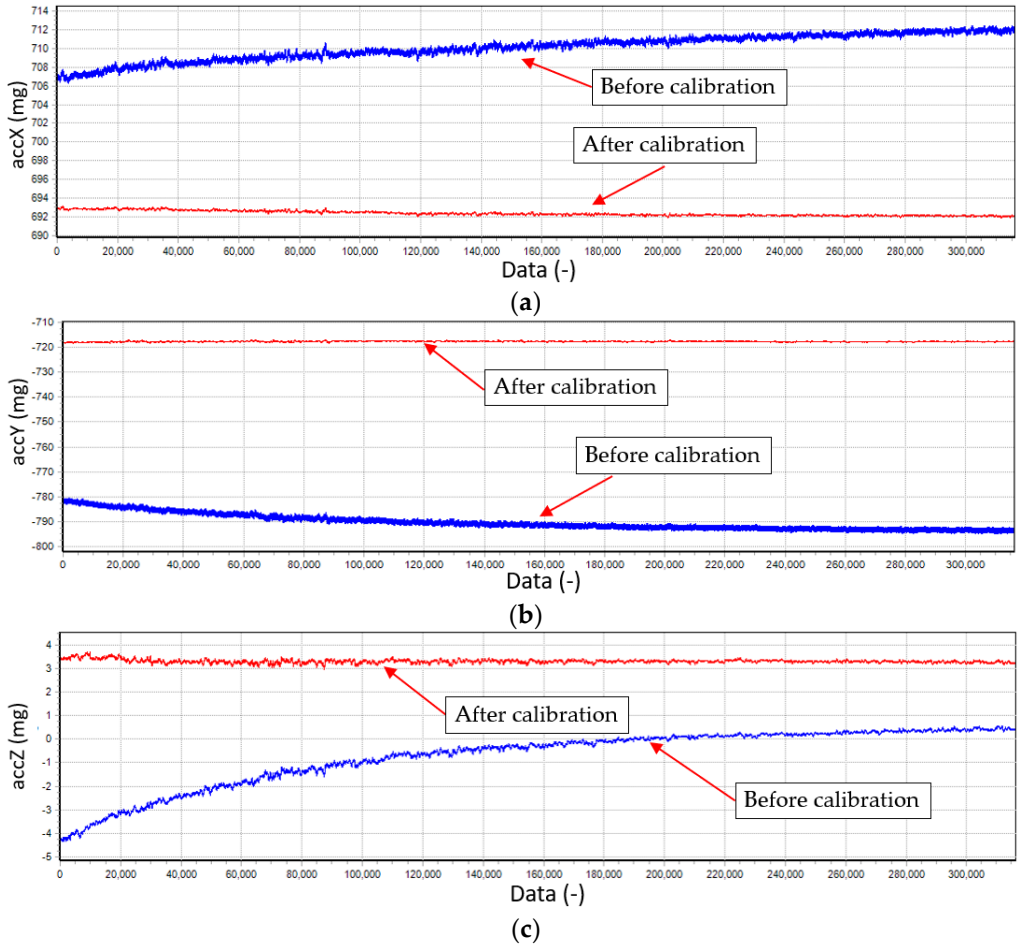

Figure 10. Dependence of Temperature before (blue line) and after (red line) calibration. (a) Thermal calibration of the x-axis. (**b**)Thermal calibration of the y-axis. (**c**) Thermal calibration of the z-axis.

 doi:10.20944/preprints202212.0339.v1

5. Conclusions

The main motivation of this paper is to analyze the validity of calibration and temperature compensation methods. We evaluated the SFEM for the ADXL355 accelerometer based on the Levenberg-Marquardt (LM) algorithm and polynomial methods. Ideally, the value of the triaxial accelerometer should be equal to the gravitational force in the static case, whether the temperature conditions are considered or not. The LM algorithm proposed in this paper is robust and efficient for the calibration of triaxial accelerometers. To compensate for thermal changes, the temperature compensation method was used combined with real-time temperature monitoring to model and incorporate temperature-related drift characteristics. Various experiments were performed to demonstrate different aspects of calibration and temperature compensation, for example, how many positions must be used to achieve the accuracy we require and how to prove the effectiveness of temperature compensation. And the experimental results show that this calibration method is effective in reducing positioning calculation errors. In all cases, there is an improvement of about 100 times after calibration, and the variation of the error parameters is reduced by almost 80% after temperature compensation. All results demonstrate the applicability of the proposed calibration and temperature compensation methods.

Some improvements can be made to the model of the triaxial accelerometer. When using the thermal calibration method to calculate the bias, scale factor, and misalignment errors at each temperature point, the results may be inaccurate since the sensor takes a long time to stabilize at the temperature being measured. More circumstances, such as input accelerations and temperature change rates that fluctuate over time, should be considered in the future. Therefore, multiple thermal models calibrated in various ambient temperatures should be developed, and a combined thermal model might be employed for demanding applications.

Author Contributions: Conceptualization, Bo Yuan; Formal analysis, Bo Yuan; Funding acquisition, Zhifeng Tang and Fuzai Lv; Methodology, Bo Yuan; Project administration, Zhifeng Tang, Pengfei Zhang and Fuzai Lv; Software, Bo Yuan; Supervision, Zhifeng Tang, Pengfei Zhang and Fuzai Lv; Validation, Bo Yuan; Visualization, Pengfei Zhang; Writing – original draft, Bo Yuan; Writing – review & editing, Zhifeng Tang.

Funding: This research received no external funding.

Institutional Review Board Statement: Not applicable.

Informed Consent Statement: Not applicable.

Data Availability Statement: The original signals and test signals presented in this study are available on request from the corresponding author.

Conflicts of Interest: The authors declare no conflict of interest.

References

1. Liu Q. Human motion state recognition based on MEMS sensors and Zigbee network[J]. Computer Communications, 2022, 181: 164-172.
2. Johnson B, Albrecht C, Braman T, et al. Development of a navigation-grade MEMS IMU[C]//2021 IEEE International Symposium on Inertial Sensors and Systems (INERTIAL). IEEE, 2021: 1-4.
3. Fontanarosa D, Francioso L, De Giorgi M G, et al. MEMS Vaporazing Liquid Microthruster: A Comprehensive Review[J]. Applied Sciences, 2021, 11(19): 8954.
4. Gaber K, El_Mashade M B, Aziz G A A. Hardware-in-the-loop real-time validation of micro-satellite attitude control[J]. Computers & Electrical Engineering, 2020, 85: 106679.
5. Iasechko M, Shelukhin O, Maranov A, et al. Evaluation of the use of inertial navigation systems to improve the accuracy of object navigation[J]. International Journal of Computer Science & Network Security, 2021, 21(3): 71-75.
6. Morales J J, Khalife J, Abdallah A A, et al. Inertial navigation system aiding with Orbcomm LEO satellite Doppler measurements[C]//Proceedings of the 31st International Technical Meeting of the Satellite Division of The Institute of Navigation (ION GNSS+ 2018). 2018: 2718-2725.

7. Al-Masri W M F, Abdel-Hafez M F, Jaradat M A. Inertial navigation system of pipeline inspection gauge[J]. IEEE Transactions on Control Systems Technology, 2018, 28(2): 609-616.
8. Zhu M, Pang L, Xiao Z, et al. Temperature drift compensation for High-G MEMS accelerometer based on RBF NN improved method[J]. Applied Sciences, 2019, 9(4): 695.
9. Wang Y, Zhang J, Yao Z, et al. A MEMS resonant accelerometer with high performance of temperature based on electrostatic spring softening and continuous ring-down technique[J]. IEEE Sensors Journal, 2018, 18(17): 7023-7031.
10. He J, Zhou W, Yu H, et al. Structural designing of a MEMS capacitive accelerometer for low temperature coefficient and high linearity[J]. Sensors, 2018, 18(2): 643.
11. Wang X, Xu W, Lee Y K. An ambient temperature compensated microthermal convective accelerometer with high sensitivity stability[C]//2019 20th International Conference on Solid-State Sensors, Actuators and Microsystems & Eu-rosensors XXXIII (TRANSDUCERS & EUROSENSORS XXXIII). IEEE, 2019: 1827-1830.
12. Wang S, Zhu W, Shen Y, et al. Temperature compensation for MEMS resonant accelerometer based on genetic algorithm optimized backpropagation neural network[J]. Sensors and Actuators A: Physical, 2020, 316: 112393.
13. Cui S, Cui L, Du Y, et al. Calibration of MEMS accelerometer using kaiser filter and the ellipsoid fitting method[C]//2018 37th Chinese Control Conference (CCC). IEEE, 2018: 4679-4684.
14. T. Xu, X. Xu, D. Xu, and H. Zhao, "A novel calibration method using six positions for MEMS triaxial accelerometer," IEEE Trans. Instrum. Meas., vol. 70, 2021, Art. no. 1002211.
15. Chao C, Zhao J, Zhu J, et al. Minimum settings calibration method for low-cost triaxial IMU and magnetometer[J]. Measurement Science and Technology, 2021, 33(2): 025103.
16. Zhu J, Wang W, Huang S, et al. An improved calibration technique for mems accelerometer-based inclinometers[J]. Sensors, 2020, 20(2): 452.
17. Ngoh K J H, Gouwanda D, Gopalai A A, et al. Estimation of vertical ground reaction force during running using neural network model and uniaxial accelerometer[J]. Journal of biomechanics, 2018, 76: 269-273.
18. Khankalantary S, Ranjbaran S, Ebadollahi S. Simplification of calibration of low-cost MEMS accelerometer and its temperature compensation without accurate laboratory equipment[J]. Measurement Science and Technology, 2021, 32(4): 045102.
19. Tkalich V L, Labkovskaia R I, Pirozhnikova O I, et al. Analysis of errors in micromechanical devices[C]//2018 XIV In-ternational Scientific-Technical Conference on Actual Problems of Electronics Instrument Engineering (APEIE). IEEE, 2018: 272-276.
20. Zhao H, Wang Y, Liu R, et al. Calibration of Smartphone's Integrated Magnetic and Inertial Measurement Units[C]//2021 33rd Chinese Control and Decision Conference (CCDC). IEEE, 2021: 7156-7161.
21. Chang H T, Chang J Y. Iterative robust ellipsoid fitting based on M-estimator with geometry radius constraint[J]. IEEE Sensors Journal, 2022.
22. Ibrahim A, Eltawil A, Na Y, et al. Accuracy limits of embedded smart device accelerometer sensors[J]. IEEE Transactions on Instrumentation and Measurement, 2020, 69(8): 5488-5496.
23. Shen Q, Yang D, Zhou J, et al. A Measurement-Data-Driven Control Approach towards Variance Reduction of Micromachined Resonant Accelerometer under Multi Unknown Disturbances[J]. Micromachines, 2019, 10(5): 294.
24. Hoang M L, Pietrosanto A. A new technique on vibration optimization of industrial inclinometer for MEMS accelerometer without sensor fusion[J]. IEEE Access, 2021, 9: 20295-20304.
25. Kose T, Azgin K, Akin T. Temperature compensation of a capacitive MEMS accelerometer by using a MEMS oscillator[C]//2016 IEEE International Symposium on Inertial Sensors and Systems. IEEE, 2016: 33-36.
26. Xu D, Yang Z, Zhao H, et al. A temperature compensation method for MEMS accelerometer based on LM_BP neural network[C]//2016 IEEE SENSORS. IEEE, 2016: 1-3.
27. Xu L, Wang S, Jiang Z, et al. Programmable synchronization enhanced MEMS resonant accelerometer[J]. Microsystems & nanoengineering, 2020, 6(1): 1-10.
28. Jalal A, Quaid M A K, Tahir S B, et al. A study of accelerometer and gyroscope measurements in physical life-log activities detection systems[J]. Sensors, 2020, 20(22): 6670.
29. Migueles J H, Rowlands A V, Huber F, et al. GGIR: a research community–driven open source R package for generating physical activity and sleep outcomes from multi-day raw accelerometer data[J]. Journal for the Measurement of Physical Behaviour, 2019, 2(3): 188-196.
30. John D, Tang Q, Albinali F, et al. An open-source monitor-independent movement summary for accelerometer data processing[J]. Journal for the Measurement of Physical Behaviour, 2019, 2(4): 268-281.
31. Ren S Q, Liu Q B, Zeng M, et al. Calibration method of accelerometer's high-order error model coefficients on precision centrifuge[J]. IEEE Transactions on Instrumentation and Measurement, 2019, 69(5): 2277-2286.
32. Ru X, Gu N, Shang H, et al. MEMS Inertial Sensor Calibration Technology: Current Status and Future Trends[J]. Mi-cromachines, 2022, 13(6): 879.
33. Araghi G. Temperature compensation model of MEMS inertial sensors based on neural network[C]//2018 IEEE/ION Position, Location and Navigation Symposium (PLANS). IEEE, 2018: 301-309.
34. Ranjbaran S, Ebadollahi S. Fast and precise solving of non-linear optimisation problem for field calibration of triaxial accelerometer[J]. Electronics Letters, 2018, 54(3): 148-150.
35. Wu H, Pei X, Li J, et al. An improved magnetometer calibration and compensation method based on Levenberg–Marquardt algorithm for multi-rotor unmanned aerial vehicle[J]. Measurement and Control, 2020, 53(3-4): 276-286.

 doi:10.20944/preprints202212.0339.v1

36. Cuadrado J, Michaud F, Lugrís U, et al. Using accelerometer data to tune the parameters of an extended kalman filter for optical motion capture: Preliminary application to gait analysis[J]. Sensors, 2021, 21(2): 427.
37. Särkkä O, Nieminen T, Suuriniemi S, et al. A multi-position calibration method for consumer-grade accelerometers, gyroscopes, and magnetometers to field conditions[J]. IEEE Sensors Journal, 2017, 17(11): 3470-3481.
38. Niu X, Li Y, Zhang H, et al. Fast thermal calibration of low-grade inertial sensors and inertial measurement units[J]. Sensors, 2013, 13(9): 12192-12217.
39. Yang J, Wu W, Wu Y, et al. Thermal calibration for the accelerometer triad based on the sequential multiposition ob-servation[J]. IEEE Transactions on Instrumentation and measurement, 2012, 62(2): 467-482.
40. Alfian R I, Ma'arif A, Sunardi S. Noise reduction in the accelerometer and gyroscope sensor with the Kalman filter algorithm[J]. Journal of Robotics and Control (JRC), 2021, 2(3): 180-189.
41. Wang Y, Li Z, Li X. External disturbances rejection for vector field sensors in attitude and heading reference systems[J]. Micromachines, 2020, 11(9): 803.
42. Shandhi M M H, Semiz B, Hersek S, et al. Performance analysis of gyroscope and accelerometer sensors for seismocardiography-based wearable pre-ejection period estimation[J]. IEEE journal of biomedical and health informatics, 2019, 23(6): 2365-2374.
43. Han Z, Hong L, Meng J, et al. Temperature drift modeling and compensation of capacitive accelerometer based on AGA-BP neural network[J]. Measurement, 2020, 164: 108019.
44. Xu T, Xu X, Xu D, et al. Low-Cost and Efficient Thermal Calibration Scheme for MEMS Triaxial Accelerometer[J]. IEEE Transactions on Instrumentation and Measurement, 2021, 70: 1-9.